Global Biogeochemical Cycles

Supporting Information for

Enrichment of ammonium in the future ocean threatens diatom productivity

Pearse J. Buchanan[1,2,3], Juan J. Pierella Karlusich[4,5], Robyn E. Tuerena[6], Roxana Shafiee[7], E. Malcolm S. Woodward[8], Chris Bowler[5], and Alessandro Tagliabue[2].

[1]CSIRO Environment, Hobart, 7004, Australia.

[2]Department of Earth, Ocean and Ecological Sciences, University of Liverpool; Liverpool, L69 3GP, UK.

[3]Department of Global Ecology, Carnegie Institution for Science; Stanford, CA, 94305, USA.

[4]FAS Division of Science, Harvard University, Cambridge, MA, 02138, USA.

[5]Institut de Biologie de l'École Normale Supérieure, Département de Biologie, École Normale Supérieure, CNRS, INSERM, Université de Recherche Paris Sciences et Lettres, Paris, France.

[6]Scottish Association for Marine Science; Dunstaffnage, Oban, PA37 1QA, UK.

[7]Center for the Environment, Harvard University, Cambridge, MA, 02138.

[8]Plymouth Marine Laboratory; Plymouth, PL1 3DH, UK.

Contents of this file

Additional Supporting Information (Files uploaded separately)

Data Sets S1 to S4

Introduction

In Text S1 we provide additional information on how ammonia oxidation and nitrite oxidation is computed within the ocean biogeochemical model. In Text S2 we evaluate the ocean biogeochemical model against observational nutrient and rate datasets (provided in Data S1-S4). Figures S1-S20 and Tables S1-S3 are provided to support the conclusions of the main text.

Text S1.

Nitrification in PISCES-v2 was previously treated as a one-step conversion of NH_4^+ to NO_3^- but was split into its two component steps (ammonia and nitrite oxidation) for the purposes of this study. Both steps were simulated implicitly by multiplying a maximum growth rate μ^{max} (day^{-1}) by the concentration of substrate (μM) to return a maximum potential rate (μM day^{-1}). This was then multiplied by limitation terms (L^X) representing the effect of environmental conditions to return the realized rate.

For ammonia oxidation ($[NH_4^+] \rightarrow [NO_2^-]$),

$$[NH_4^+] \rightarrow [NO_2^-] = \mu_{AO}^{max} \cdot [NH_4^+] \cdot L_{AO}^{NH_4^+} \cdot L_{AO}^{PAR} \cdot L_{AO}^{pH} \quad (1)$$

$$\mu_{AO}^{max} = \max(0.2, 0.029 \cdot T - 0.147) \quad (2)$$

$$L_{AO}^{NH_4^+} = \frac{NH_4^+}{NH_4^+ + K_{AO}^{NH_4^+}} \quad (3)$$

$$L_{AO}^{PAR} = 1 - \frac{PAR}{PAR + K_{AO}^{PAR}} \quad (4)$$

$$L_{AO}^{pH} = \min\left(1, \frac{10^{(pH - pK_a)}}{10^{(R_{pH} - pK_a)}}\right) \quad (5)$$

In the above, μ_{AO}^{max} is estimated by a linear model with a floor of 0.2 day^{-1} (Eqn. 2). This model was fit to the growth curves of three ecotypes of ammonia-oxidizing archaea (Qin et al., 2015) and returns rates of 0.8 day^{-1} near 30°C (Fig. S20). A floor of 0.2 day^{-1} was justified by relatively high rates observed in near-freezing waters (Tolar et al., 2016). The limitation term for NH_4^+ uptake ($L_{AO}^{NH_4^+}$, Eqn. 3) assumes a constant half-saturation coefficient $K_{AO}^{NH_4^+}$ of 0.1 μM, which is well reflective of both natural marine assemblages of archaea (Horak et al., 2013; Newell et al., 2013; Olson, 1981; Peng et al., 2016;

Xianhui Sean Wan et al., 2018) and the cultivated archaea *Nitrosopumilus maritimus* SCM1 (Martens-Habbena et al., 2009). Light limitation (L_{AO}^{PAR}) and effects of pH (L_{AO}^{pH}) are less well constrained, but nonetheless important. We set the half saturation term of photoinhibition (K_{AO}^{PAR}, Eqn. 4) to 0.75 W m^{-2}, which accounted for an 80% reduction in rates at photosynthetically active radiation levels of 3 W m^{-2} (Merbt et al., 2012). We set the reference pH (R_{pH}, Eqn. 5) below which negative effects on oxidation occur at 8.0, which reflects surface conditions of historical ocean and therefore the pH (i.e., NH_3 availability) that ammonia oxidizers are likely adapted to (Ward, 1987). With a pK_a of the NH_3-NH_4^+ equilibrium equal to 9.3 (Zeebe & Wolf-Gladrow, 2001), this treatment reduced oxidation rates by 27.5% for a decline in pH of 0.14 units, which is a more conservative change than the 36-38% declines in oxidation reported by Beman et al. (2011) for the same pH change.

For nitrite oxidation ($[NO_2^-] \rightarrow [NO_3^-]$),

$$[NO_2^-] \rightarrow [NO_2^-] = \mu_{NO}^{max} \cdot [NO_2^-] \cdot L_{NO}^{NO_2^-} \cdot L_{NO}^{PAR} \quad (6)$$

$$L_{NO}^{NO_2^-} = \frac{NO_2^-}{NO_2^- + K_{NO}^{NO_2^-}} \quad (7)$$

$$L_{NO}^{PAR} = 1 - \frac{PAR}{PAR + K_{AO}^{PAR}} \quad (8)$$

The treatment of nitrite oxidation is like ammonia oxidation. However, there are two key differences. First, nitrite-oxidizing bacteria have lower growth yield per unit nitrogen oxidized compared to ammonia-oxidizing archaea (Bayer et al., 2022), which demands a slower growth rate in our model given that we are simulating this metabolism implicitly. Accordingly, we set the maximum growth rate of nitrite-oxidizing bacteria (μ_{NO}^{max}) to a constant 0.15 day^{-1}, informed by doubling times in excess of four days of marine cultures held at optimal conditions (Spieck & Lipski, 2011). Second, pH has no effect on NO_2^- concentrations. Otherwise, we maintain the same half-saturation coefficients for the substrate ($L_{NO}^{NO_2^-}$, Eqn. 7) and light limitation (L_{NO}^{PAR}, Eqn. 8) terms as for ammonia oxidizers, being 0.1 µM for $K_{NO}^{NO_2^-}$ and 0.75 W m^{-2} for K_{NO}^{PAR} (Table S3). All parameters for nitrification are presented in Table S3.

We did not include oxygen or iron limitation. Oxygen was ignored due to reports of high activity and biomass of nitrifiers in low oxygen zones, due perhaps to a combination of high cellular affinity for oxygen (Bristow et al., 2016) and potential anaerobic pathways of oxidation via alternative electron acceptors (Babbin et al., 2020; Kraft et al., 2022). We ignored iron limitation, despite its potential for limiting growth of ammonia oxidizers (Shafiee et al., 2019), because little is known regarding its effects on the growth of nitrite-oxidizing bacteria. In addition, changes to the availability of iron for biology in the future ocean are highly uncertain and models have little skill in this regard (Tagliabue et al., 2016). We acknowledge, however, that changes in both oxygen and iron availability may be important additional factors governing shifts in the NH_4^+ to DIN ratio in a future ocean.

Text S2.

Observations show that NH_4^+ concentrations of 0.1 μM or greater exist over continental shelves and in regions of strong mixing with high rates of primary production and subsequent heterotrophy. This accumulation of NH_4^+ in productive regions is reproduced by our model (Fig S2a). However, as high NH_4^+ co-occurs with high NO_3^- concentrations, NH_4^+ makes a small contribution to total DIN in these upwelling systems (Fig. S2b), which include the eastern tropical Pacific, eastern boundary upwelling systems, the northwest Indian Ocean, the subpolar gyres and the Southern Ocean (although the model underestimates NH_4^+ concentrations in the Southern Ocean). In contrast, low NH_4^+ concentrations of less than 0.05 μM pervade the oligotrophic gyres of the lower latitudes. As these regions also display very low NO_3^- concentrations, NH_4^+ makes up a much higher fraction of total DIN in both the observations and our model, with the NH_4^+ peak occurring deeper in the water column (Fig. S3).

Eutrophic upwelling systems and oligotrophic waters differed in the major sinks of NH_4^+ (Fig. S1), consistent with available observations and constraints from theory. In eutrophic waters (defined by surface nitrate > 1 μM), ammonia oxidation represented 49 ± 29 % (mean ± standard deviation) of NH_4^+ sinks, but this dropped to 32 ± 9 % in oligotrophic systems. Measured rates of ammonia oxidation showed a positive relationship with surface NO_3^- concentrations and this was reproduced by the model (Fig.

S4), indicating that ammonia oxidation was indeed a greater proportion of the overall NH_4^+ budget in eutrophic regions. In agreement, isotopic methods have shown that the bulk of nitrogen assimilated by phytoplankton in oligotrophic waters is recycled (Eppley & Peterson, 1979; Fawcett et al., 2011; Klawonn et al., 2019; Van Oostende et al., 2017; Xianhui S. Wan et al., 2021), implying that most nitrogen cycling occurs without ammonia oxidation. Again, our model reproduces this feature of oligotrophic systems (Fig. S1).

Parallel observations of NH_4^+ to DIN ratios and rates of new and regenerated production from studies spanning tropical to polar environments (Fernández et al., 2009; Joubert et al., 2011; Mdutyana et al., 2020; Metzler et al., 1997; Philibert, 2015; Rees et al., 2006; Thomalla et al., 2011; Xianhui Sean Wan et al., 2018; Yingling et al., 2021) show that there is a strong relationship between the NH_4^+ to DIN ratio and the proportion of primary production that is regenerated (Fig. S6). This relationship is expected, in that high NH_4^+ to DIN ratios should coincide with high rates of regenerated primary production. However, the nature of this relationship was sharp, and was well described by a quadratic Monod function with an optimal half-saturation constant of 0.2 ± 0.03 and an exponent of 0.5 ± 0.05 (Pearson's correlation = 0.69; R^2 (coefficient of determination) = 0.47; as compared to a linear relationship with an R^2 (coefficient of determination) = -1.13)). This quadratic function predicts that regenerated production contributes half of total net primary production when the standing stock of NH_4^+ is only 4 ± 3 % of total DIN. Phytoplankton therefore grow principally on NO_3^- (new production dominates) only when NH_4^+ is substantially depleted.

A similarly sharp relationship emerges from our global ocean-biogeochemical model (Aumont et al., 2015) (grey dots in Fig. S6) equipped with diatoms as an explicit phytoplankton functional type. In the model, all phytoplankton are parameterized to have higher affinities for NH_4^+, and their growth is supported by NH_4^+ until NO_3^- becomes sufficiently enriched that higher growth can be achieved on NO_3^- (Fig. S4). However, the transition at which growth on NO_3^- accelerates (cross-over of blue and yellow lines in Fig. S4) occurs at lower concentrations of NO_3^- for diatoms than other phytoplankton. This switch to NO_3^--fueled growth for diatoms occurs at a point where they are still outcompeted by other phytoplankton for nitrogen. All else being equal, diatoms therefore

suffer from greater growth limitation in low NO_3^-, high NH_4^+ regimes. Only when NO_3^- is truly plentiful (very low NH_4^+ to DIN ratios) do diatoms achieve the high growth rates that allow them to carve out a competitive niche. While other limiting factors such as silicate, iron and light are also influential, these differences in the growth response to NH_4^+ and NO_3^-, which reflect the measured affinities of diatoms and other major taxa (Litchman et al., 2007) and the universal preference for NH_4^+ at low NO_3^- (Flynn, 1999), contribute to the dominance of diatoms in upwelling systems and their competitive exclusion in relatively NH_4^+-rich oligotrophic seas.

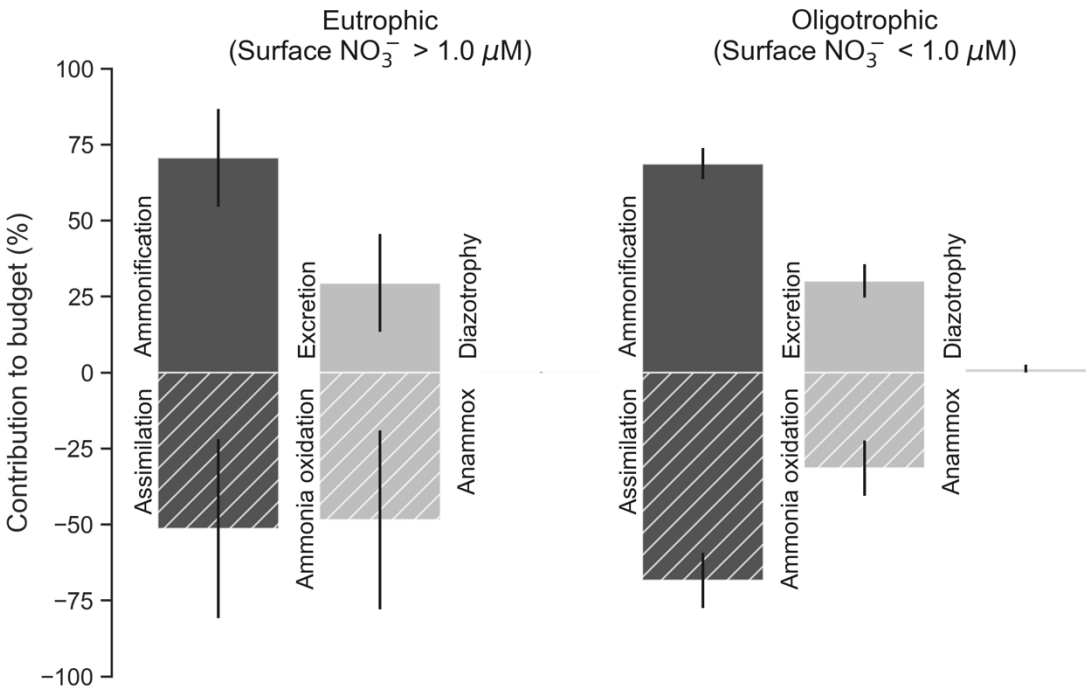

Figure S1. Global mean ± standard deviations of NH_4^+ fluxes separated into eutrophic and oligotrophic regions. Sources of NH_4^+ are represented by positive values and sinks by negative values.

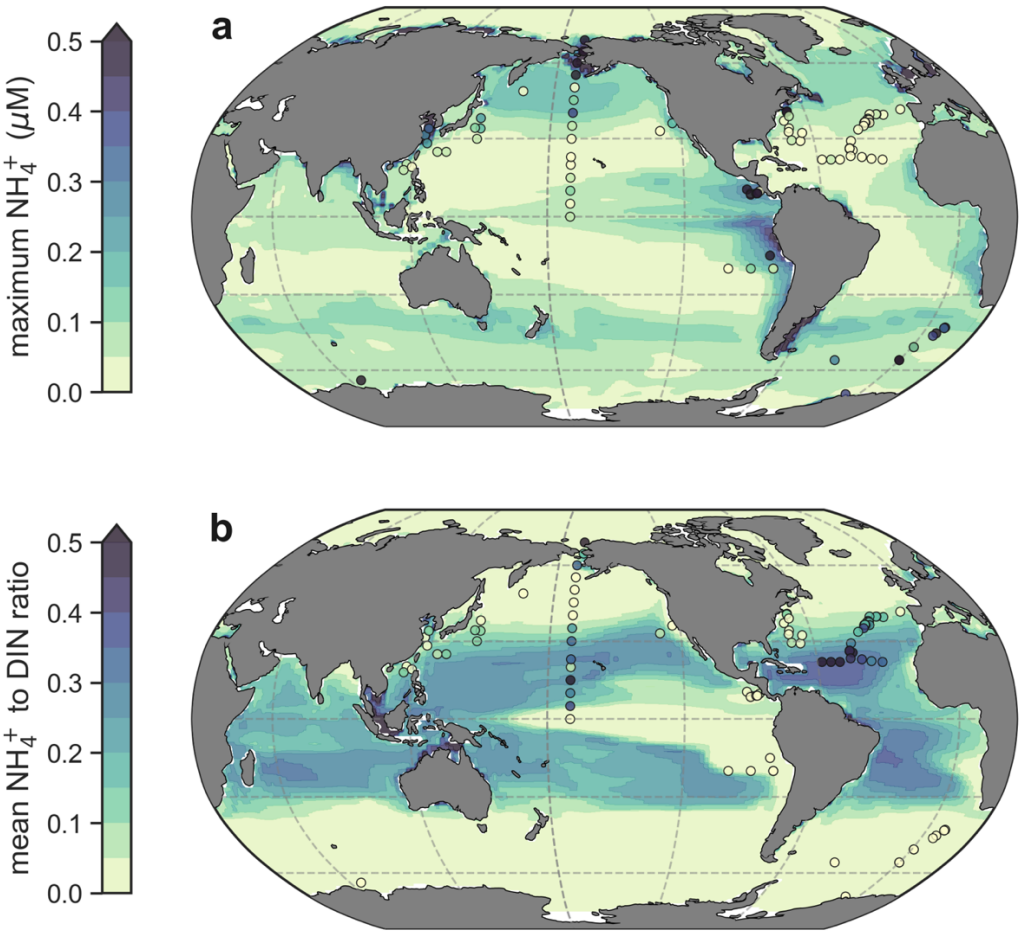

Figure S2. Global patterns of NH_4^+ concentrations and its contribution to DIN in the euphotic zone. (a) The simulated maximum NH_4^+ concentration within the euphotic zone. The maximum was chosen to emphasise basin-scale variations. (b) Average values of the NH_4^+:DIN ratio. Modelled values are annual averages of the preindustrial control simulation between years 2081-2100. Observed values following linear interpolation between the surface and 200 metres depth are overlaid as coloured markers. Only those profiles with at least 3 data points within the upper 200 metres are shown.

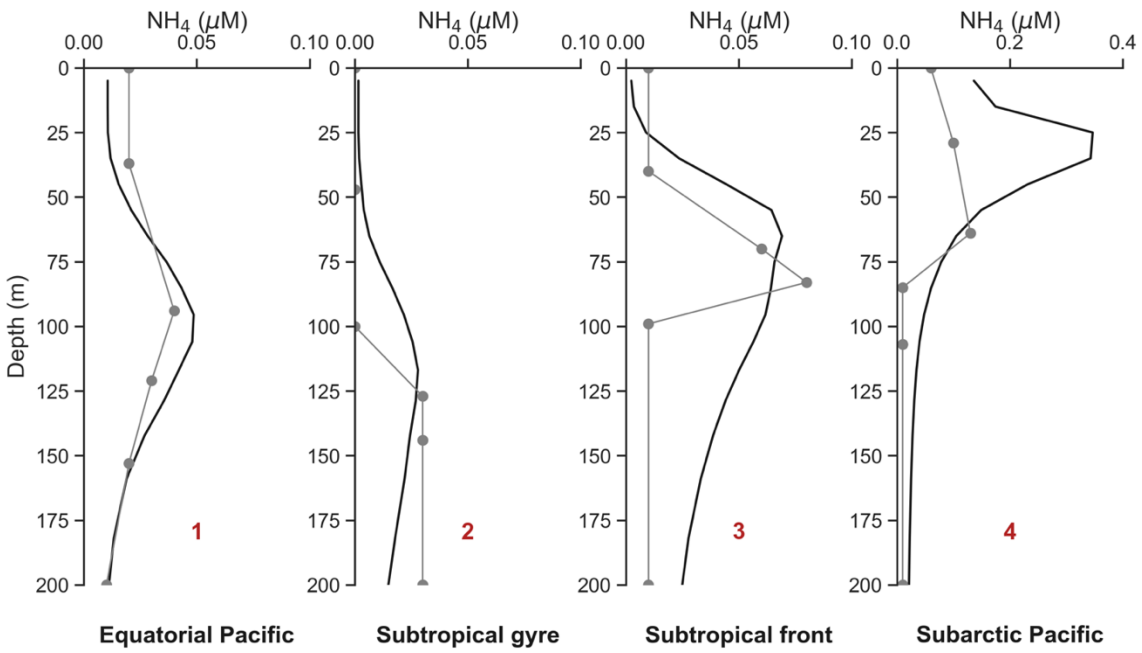

Figure S3. Simulated and observed depth profiles of NH_4^+ at four locations in the North Pacific Ocean (Shiozaki et al., 2016).

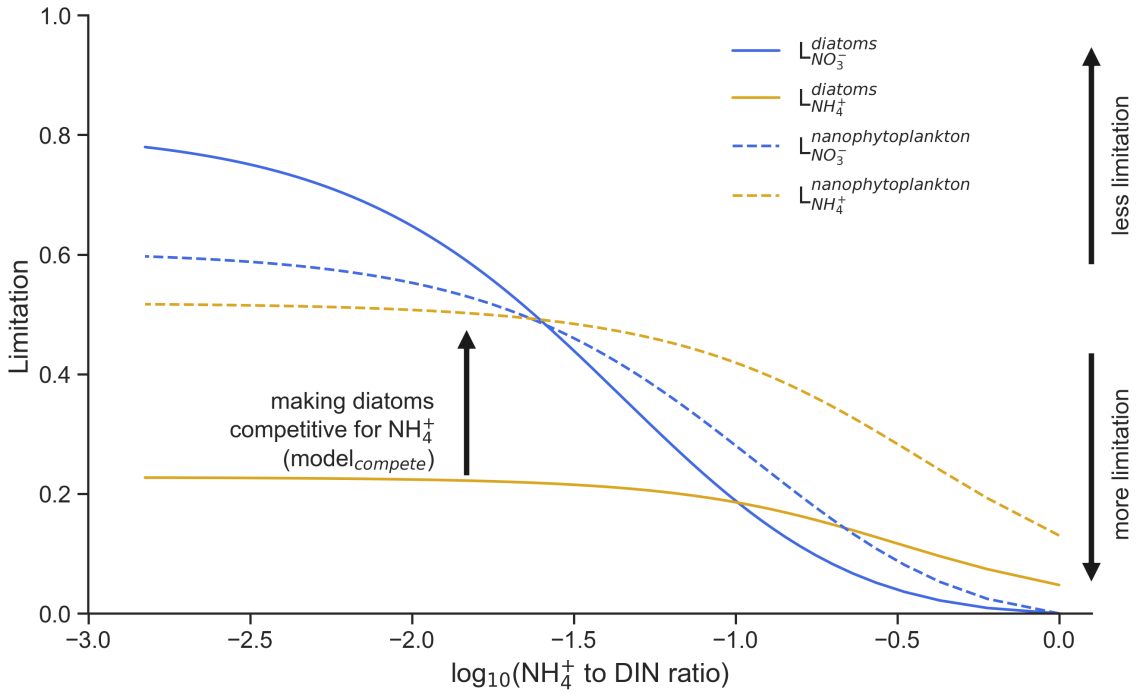

Figure S4. Limitation of diatoms (solid) and other phytoplankton (dashed) in the ocean-biogeochemical model by NO_3^- (blue) and NH_4^+ (yellow) as a function of the NH_4^+:DIN ratio on a $\log_{10}$ scale.

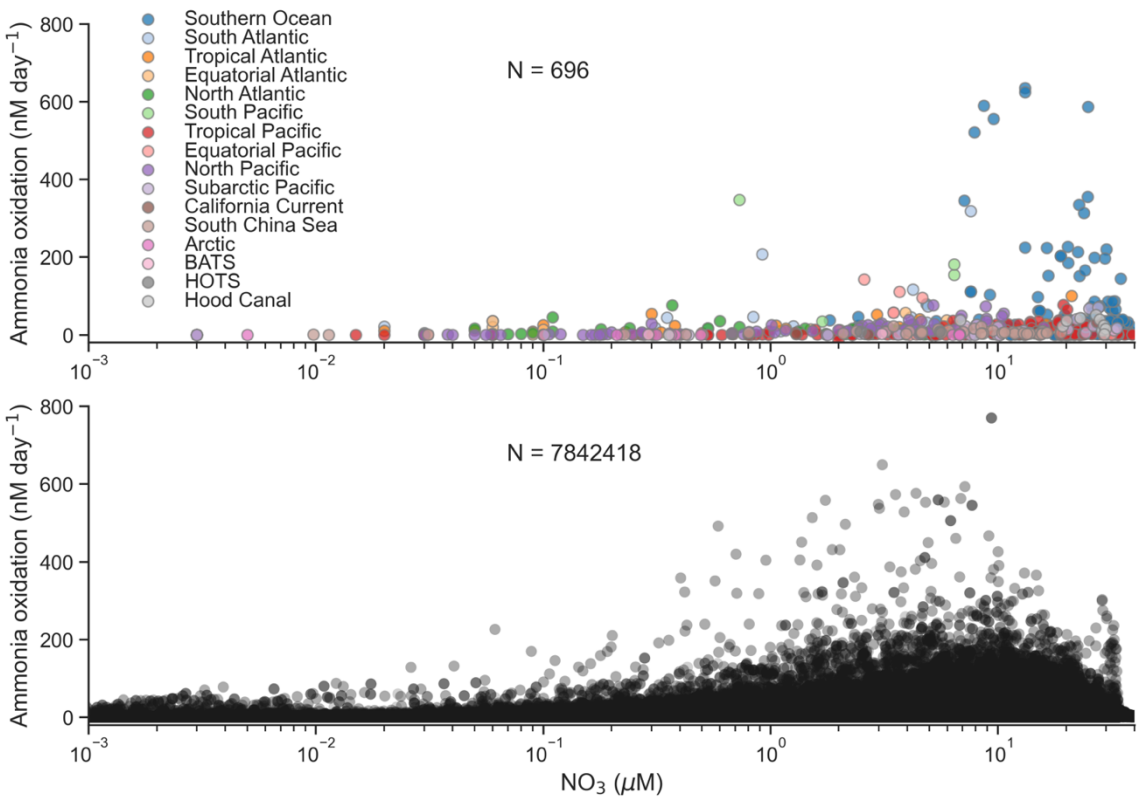

Figure S5. Measured (top) and modelled (bottom) ammonia oxidation rates from the global ocean plotted against the $\log_{10}$ of nitrate (NO_3), which indicates a spectrum of oligotrophy-eutrophy from left to right along the x-axis.

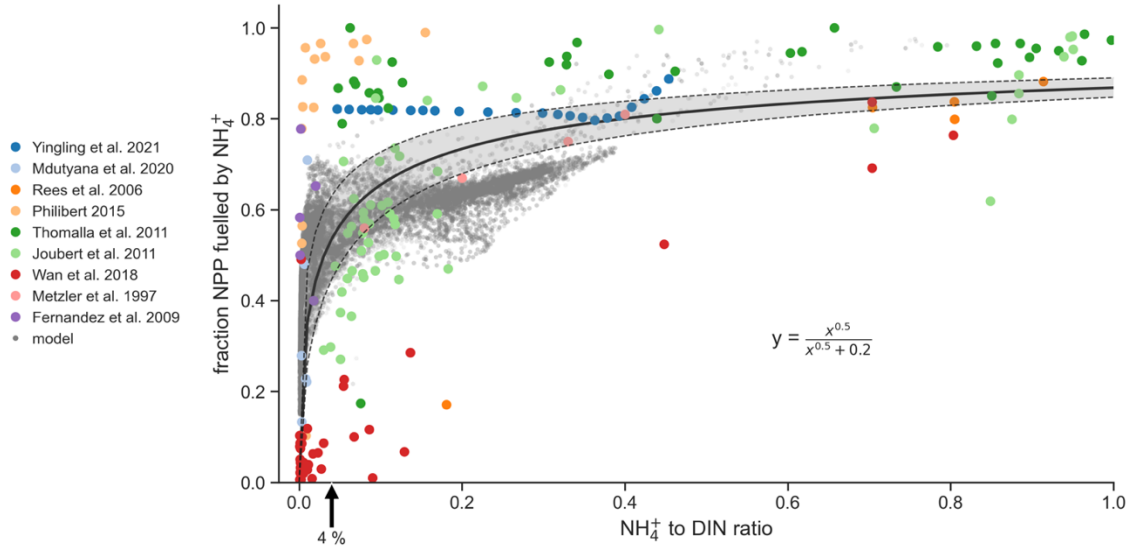

Figure S6. Coincident measurements of the NH_4^+ to DIN ratio and the fraction of NPP fuelled by NH_4^+ from 9 studies (coloured dots) and as output by the model (grey dots). Black solid line is the best fit line to the observations and is described by the equation. Shading denotes one standard deviation.

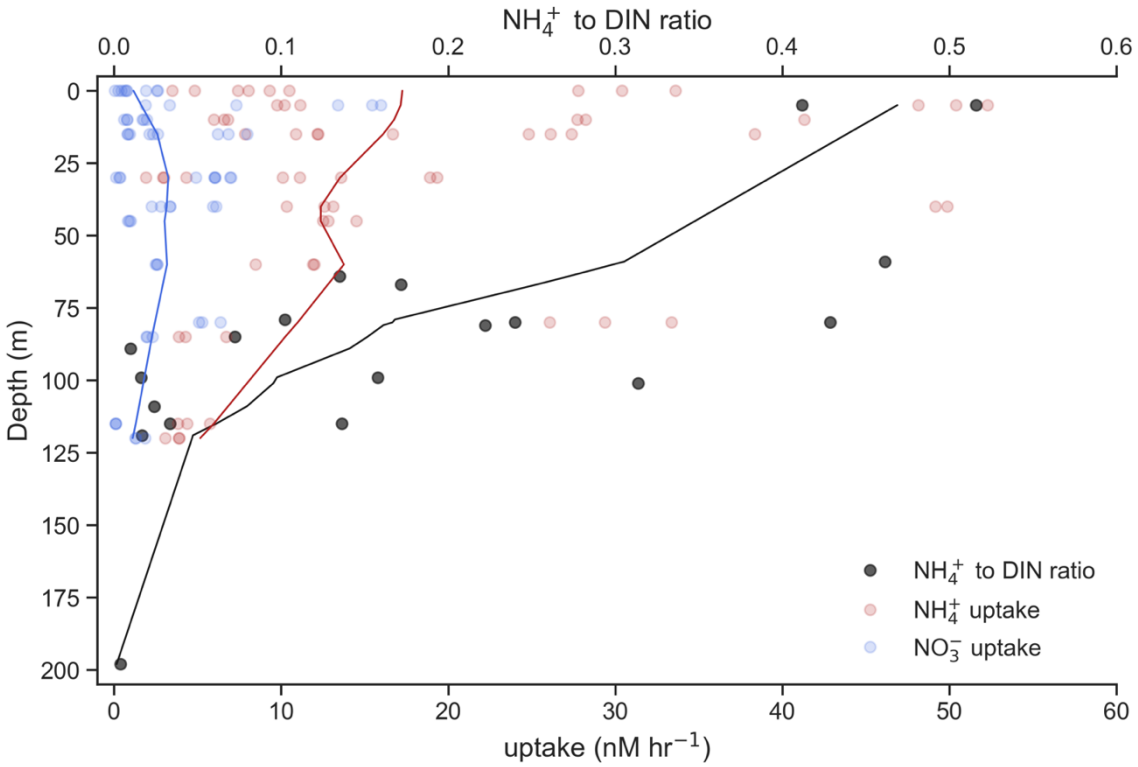

Figure S1. Nutrient and community uptake rate data from the Gulf of Mexico (Yingling et al., 2021). Linear interpolations in depth are constructed and the interpolated values are used in Figure S6.

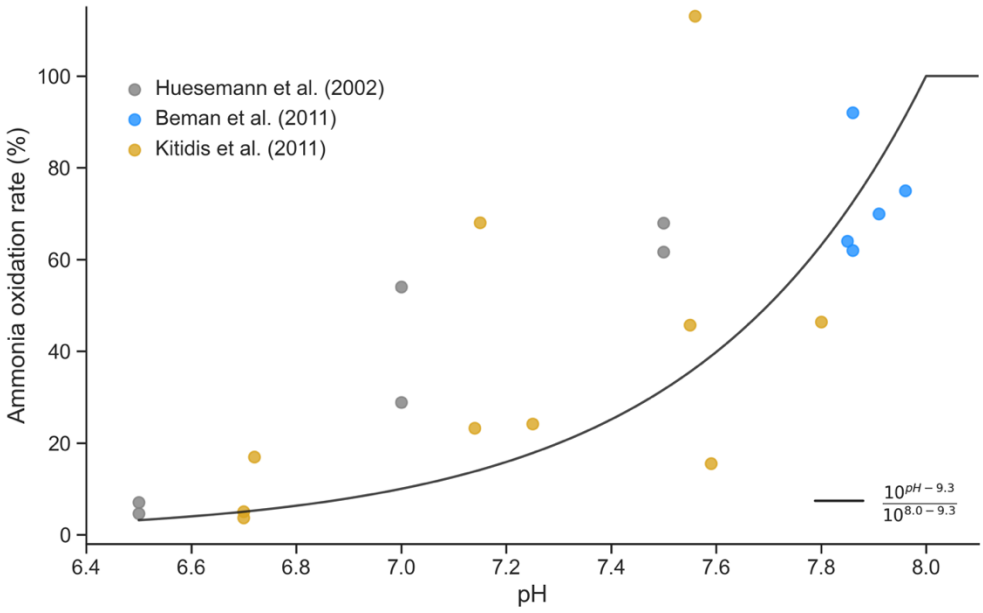

Figure S8. Parameterisation of ocean acidification on ammonia oxidation. Measurements of rate change in ammonia oxidation due to forced declines in pH (markers) are compared with a parameterisation for the relationship between pH and ammonia oxidation rate (solid line). This parameterisation returns a Pearson's correlation of 0.68 ($R^2 = 0.46$).

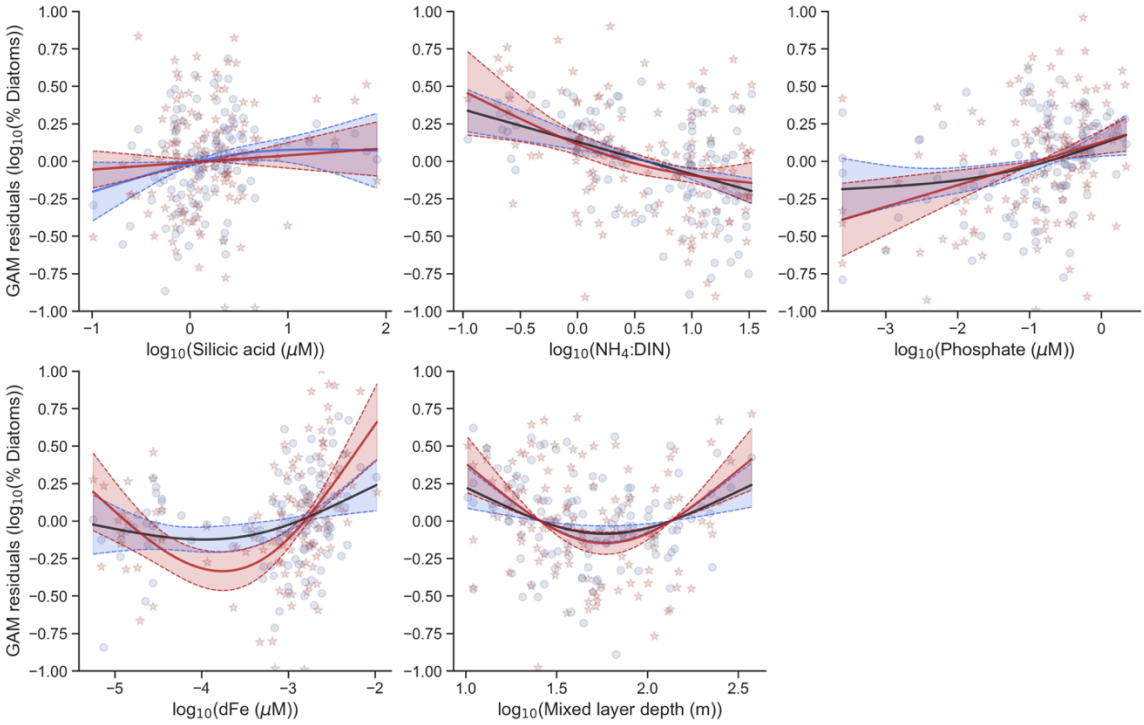

Figure S9. Key predictors of diatom relative abundance as a proportion of eukaryotic phytoplankton (blue) and all phytoplankton (red) generated by a GAM. The predictors are the $\log_{10}$ transformed silicic acid concentration (*in situ*), ratio of NH_4^+:DIN (model-derived), phosphate concentration (*in situ*), dissolved iron concentration (model-derived) and mixed layer depth (*in situ*). Dots are the partial residuals of the fitted GAM. The deviance explained and significance of each predictor are reported in Table S1.

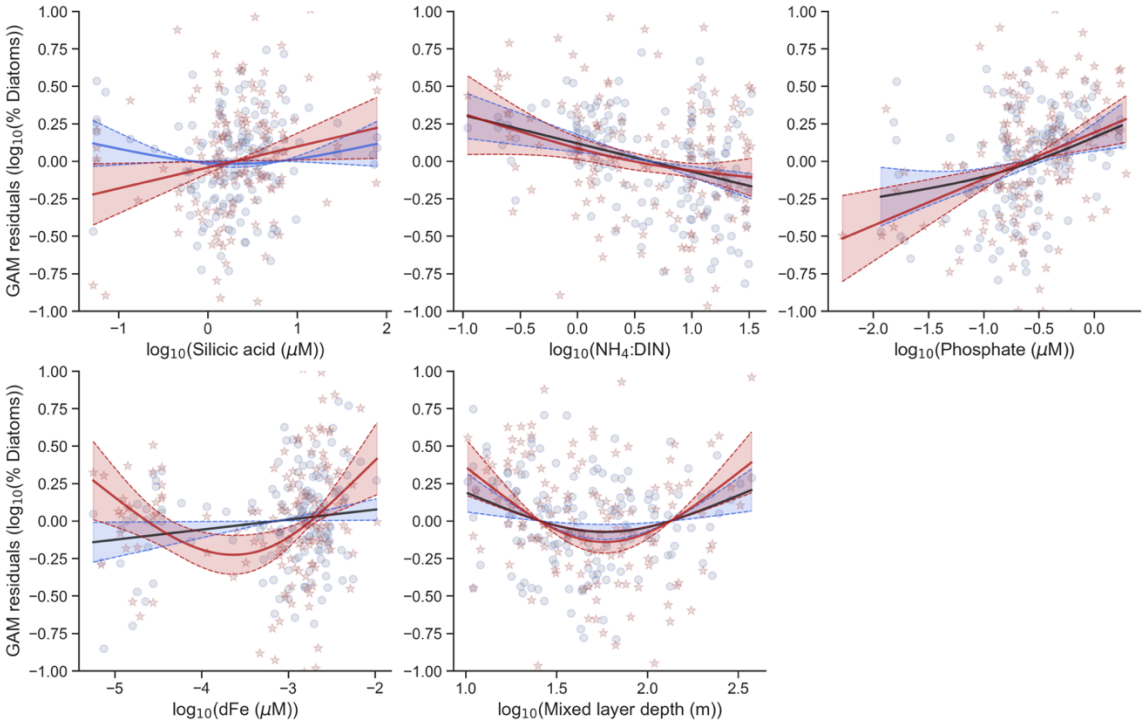

Figure S10. Key predictors of diatom relative abundance as a proportion of eukaryotic phytoplankton (blue) and all phytoplankton (red) generated by a GAM. The predictors are the $\log_{10}$ transformed silicic acid concentration (WOA18 (Garcia et al., 2019)), ratio of NH_4^+:DIN (model-derived), phosphate concentration (WOA18 (Garcia et al., 2019)), dissolved iron concentration (model-derived) and mixed layer depth (*in situ*). Dots are the partial residuals of the fitted GAM. The deviance explained and significance of each predictor are reported in Table S1.

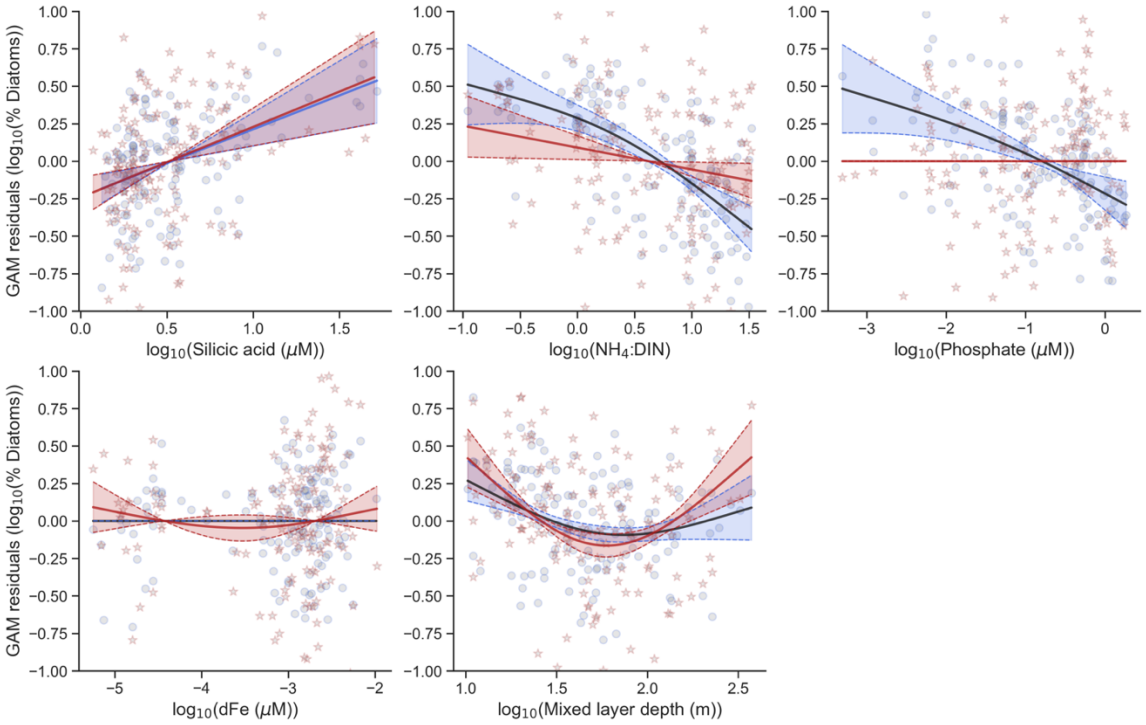

Figure S11. Key predictors of diatom relative abundance as a proportion of eukaryotic phytoplankton (blue) and all phytoplankton (red) generated by a GAM. The predictors are the $\log_{10}$ transformed silicic acid concentration (model-derived), ratio of NH_4^+:DIN (model-derived), phosphate concentration (model-derived), dissolved iron concentration (model-derived) and mixed layer depth (*in situ*). Dots are the partial residuals of the fitted GAM. The deviance explained and significance of each predictor are reported in Table S1.

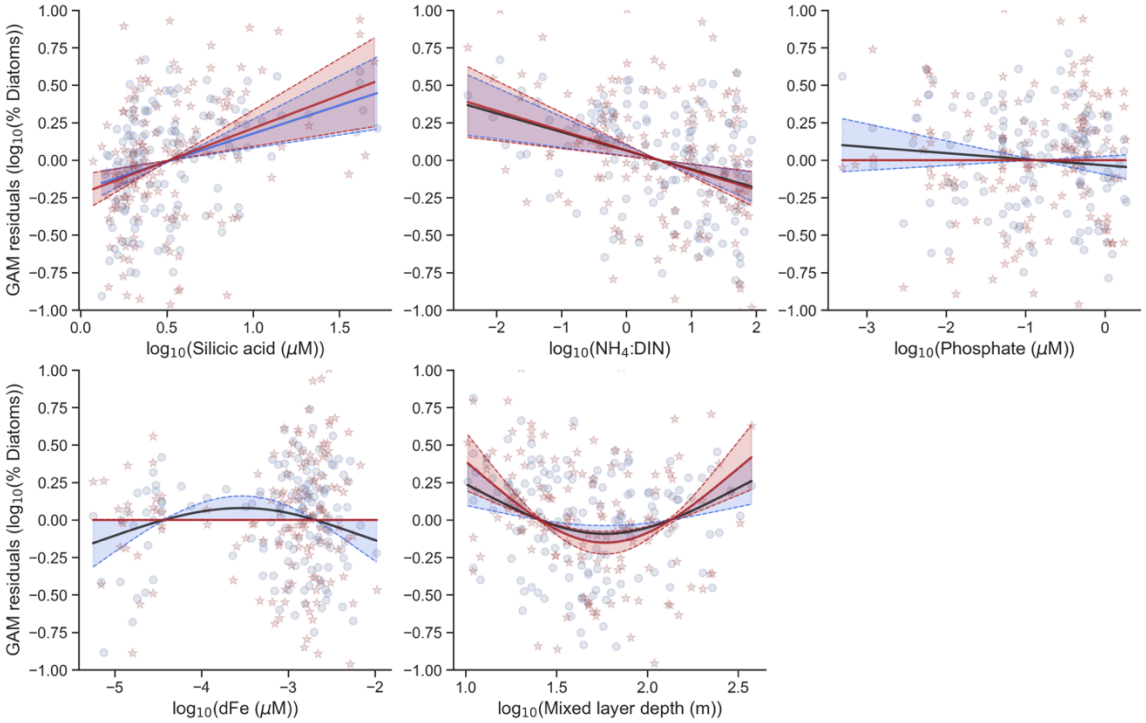

Figure S12. Key predictors of diatom relative abundance as a proportion of eukaryotic phytoplankton (blue) and all phytoplankton (red) generated by a GAM. The predictors are the $\log_{10}$ transformed silicic acid concentration (model-derived), ratio of NH_4^+:DIN (Darwin model), phosphate concentration (model-derived), dissolved iron concentration (model-derived) and mixed layer depth (*in situ*). Dots are the partial residuals of the fitted GAM. The deviance explained and significance of each predictor are reported in Table S1.

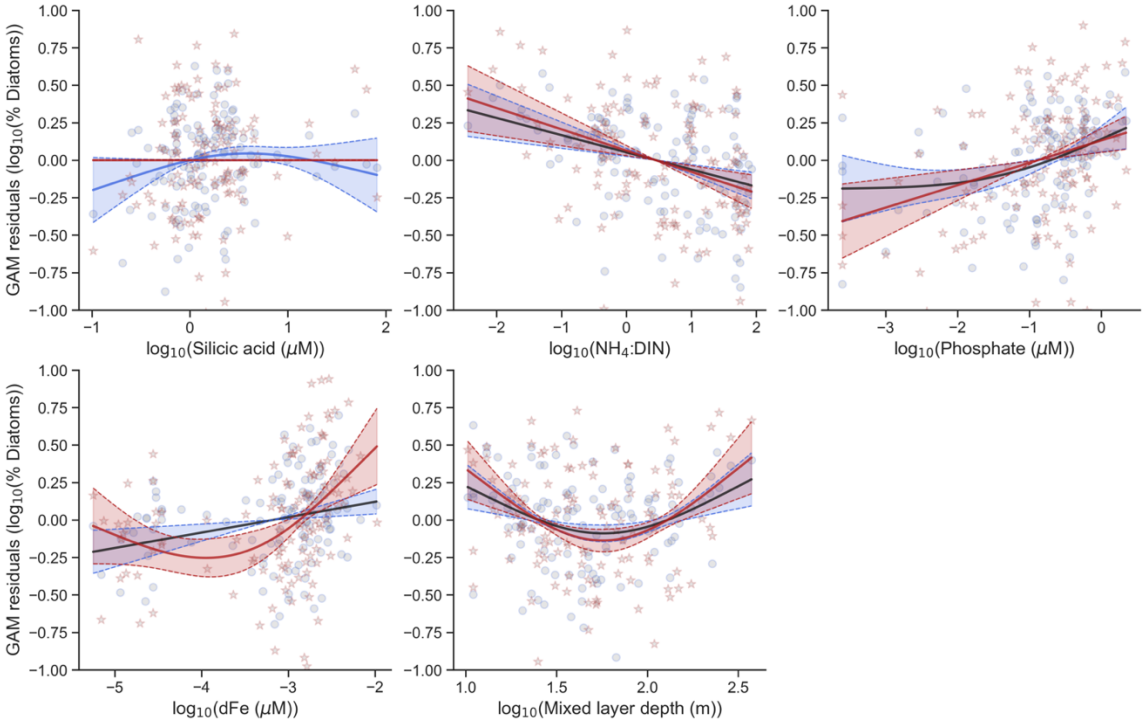

Figure S13. Key predictors of diatom relative abundance as a proportion of eukaryotic phytoplankton (blue) and all phytoplankton (red) generated by a GAM. The predictors are the $\log_{10}$ transformed silicic acid concentration (*in situ*), ratio of NH_4^+:DIN (Darwin model), phosphate concentration (*in situ*), dissolved iron concentration (model-derived) and mixed layer depth (*in situ*). Dots are the partial residuals of the fitted GAM. The deviance explained and significance of each predictor are reported in Table S1.

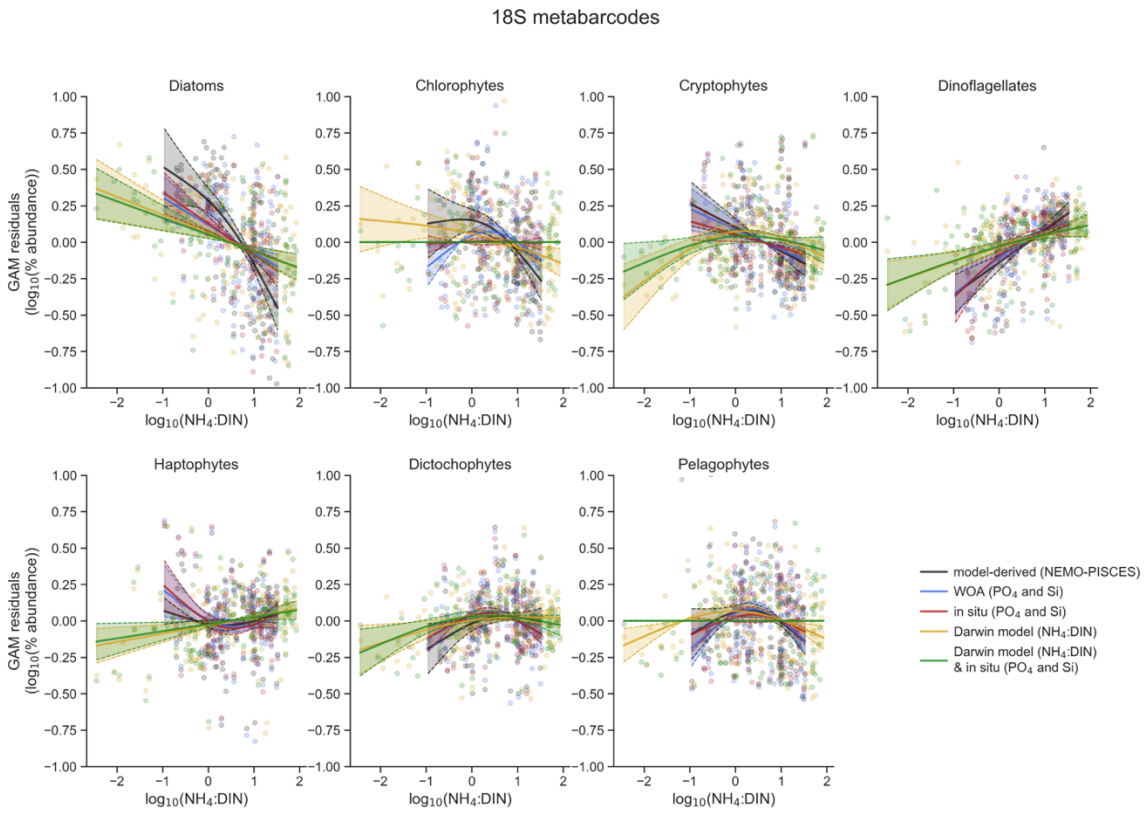

Figure S13. GAM relationships between NH_4^+ to DIN ratios and the relative abundance of each major phytoplankton taxa from the 18S metabarcoding estimates. Dots are the partial residuals of the fitted GAM. Each colour indicates a different combination of predictor variables.

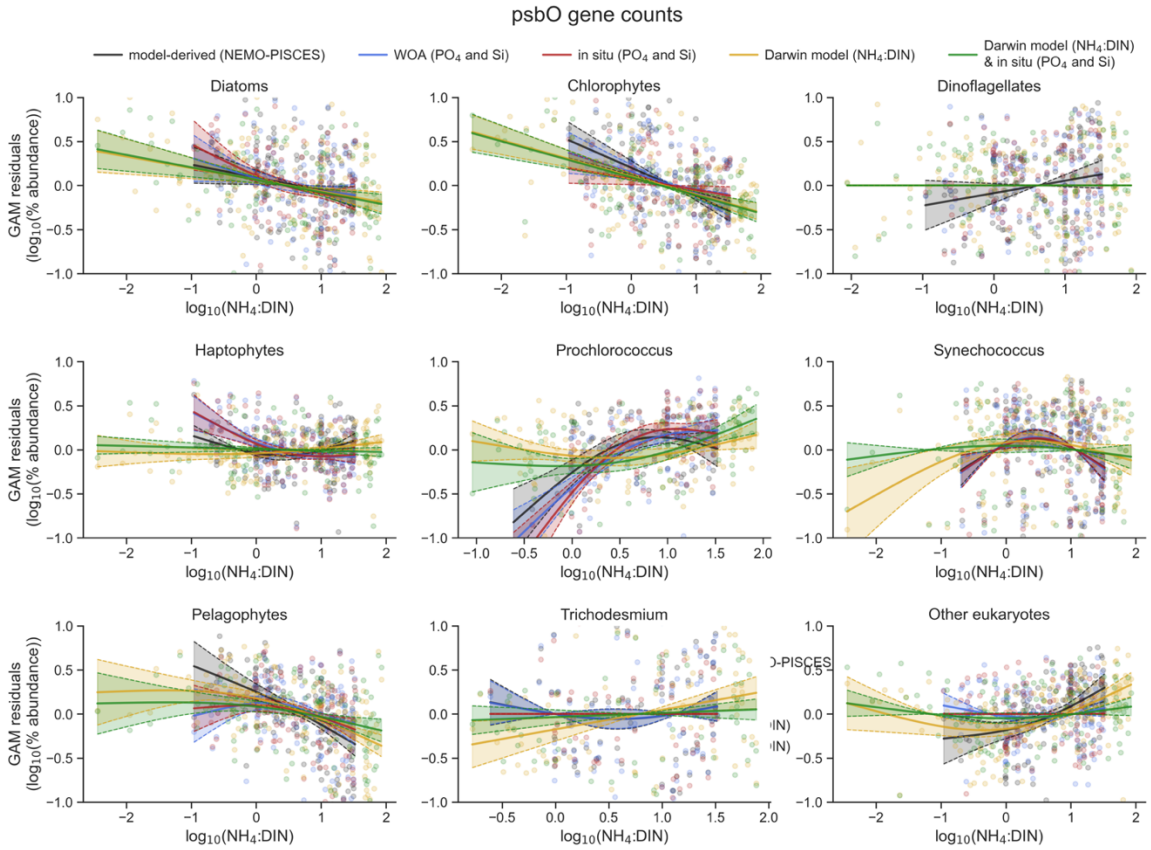

Figure S15. GAM relationships between NH_4^+ to DIN ratios and the relative abundance of each major phytoplankton taxa from the *psbO* gene count estimates. Dots are the partial residuals of the fitted GAM. Each colour indicates a different combination of predictor variables.

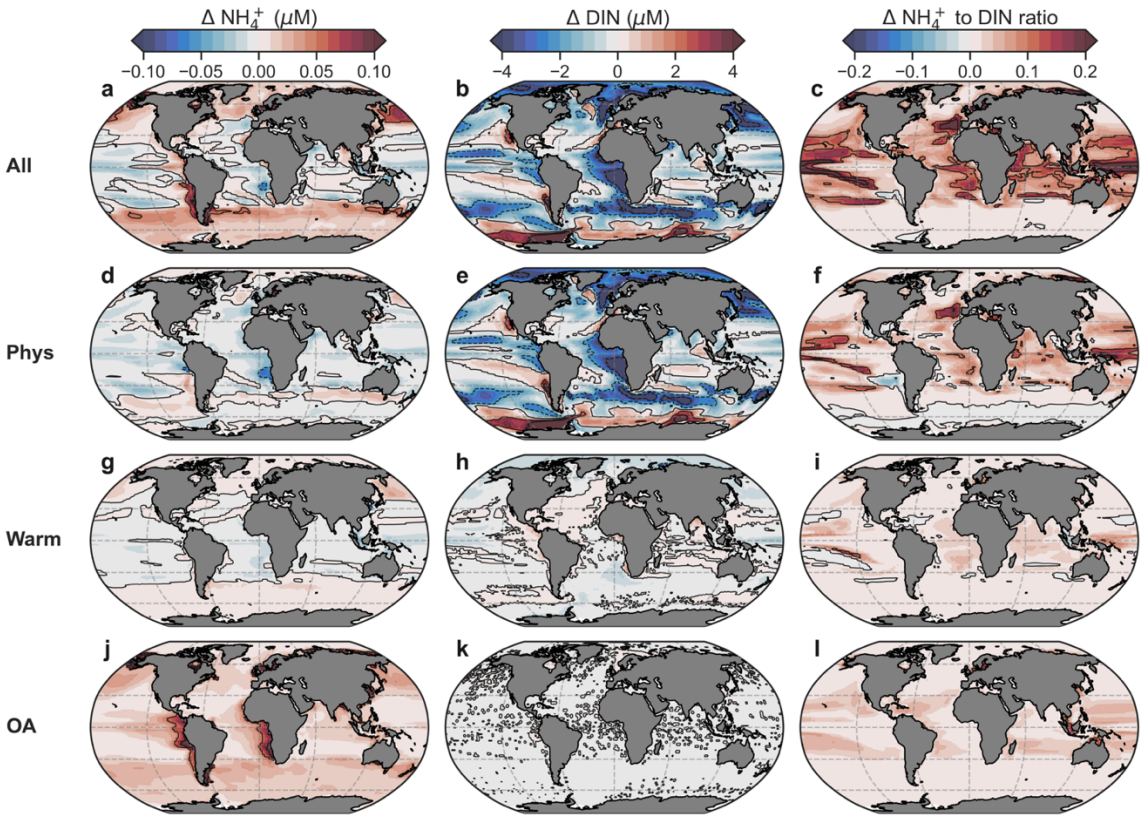

Figure S16. Anthropogenic impacts on concentrations of NH_4^+, DIN and NH_4^+:DIN ratios. a-c, The difference in concentrations and the NH_4^+ to DIN ratio averaged over the euphotic zone at the end of the 21st century (2081-2100) with all anthropogenic impacts (All). d-f, same as a-c but for physical changes (circulation + light) only (Phys). g-i, same as a-c but for warming effects on metabolism only (Warm). j-l, same as a-c but for ocean acidification only (OA).

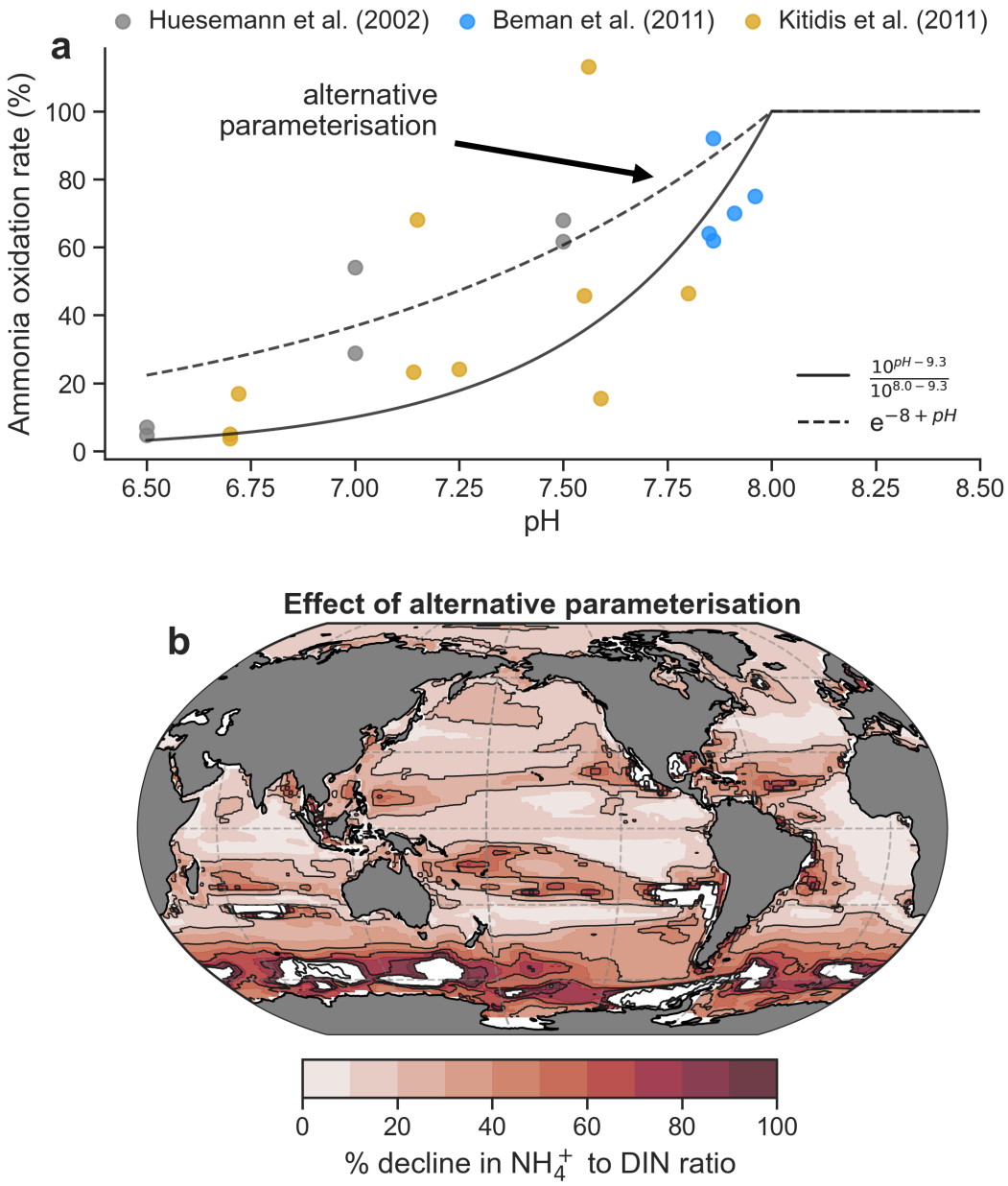

Figure S17. Alternative parameterisation of pH effect on ammonia oxidation. a, The alternative parameterisation (dashed line), which includes a weaker effect of pH decline on ammonia oxidation. b, How the weaker relationship between pH and ammonia oxidation ameliorates the increases in NH_4^+:DIN. As NH_4^+:DIN increases almost everywhere in these experiments, we only show how this alternative parameterisation works to reduce the increase.

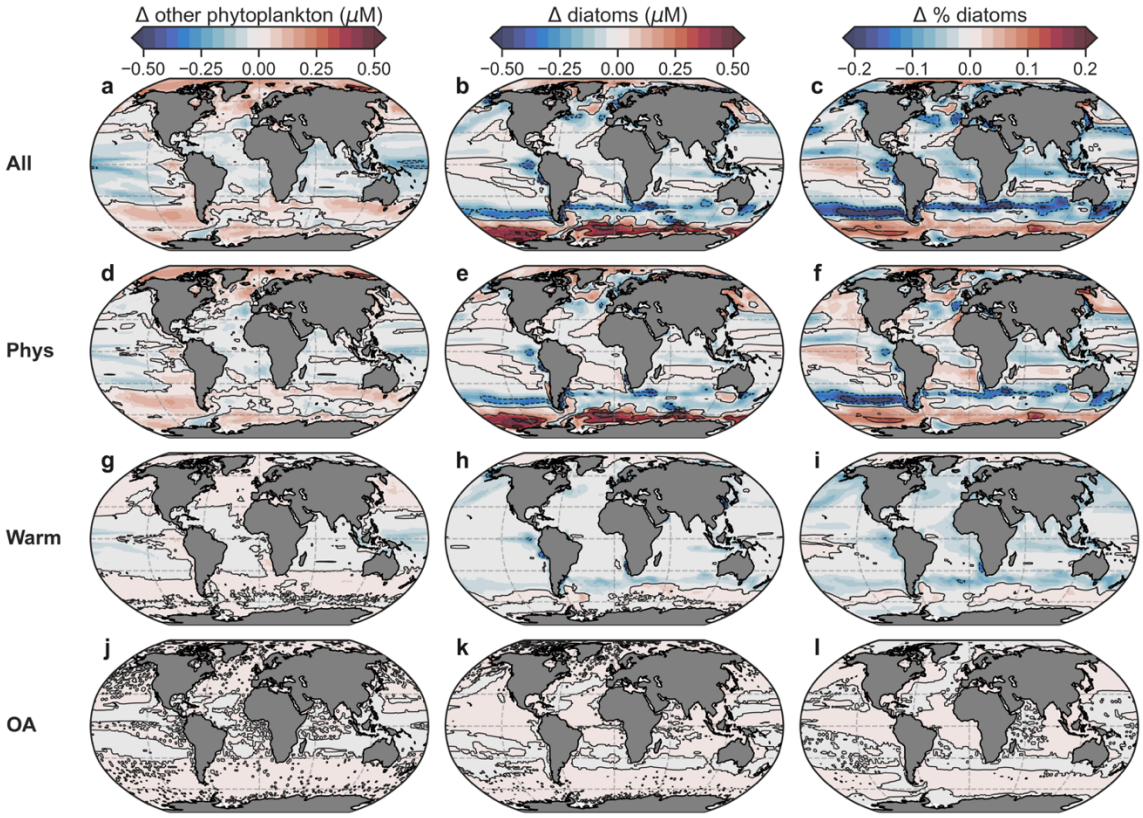

Figure S18. Anthropogenic impacts on concentrations of other phytoplankton, diatoms and the relative abundance of diatoms. a-c, Concentrations and the relative abundance of diatoms are averaged over the depths at which total phytoplankton concentrations are greater than 0.1 μM of carbon at the end of the 21st century (2081-2100) with all anthropogenic impacts (All). d-f, same as a-c but for physical changes (circulation + light) only (Circ). g-i, same as a-c but for warming effects on metabolism only (Warm). j-l, same as a-c but for ocean acidification only (OA).

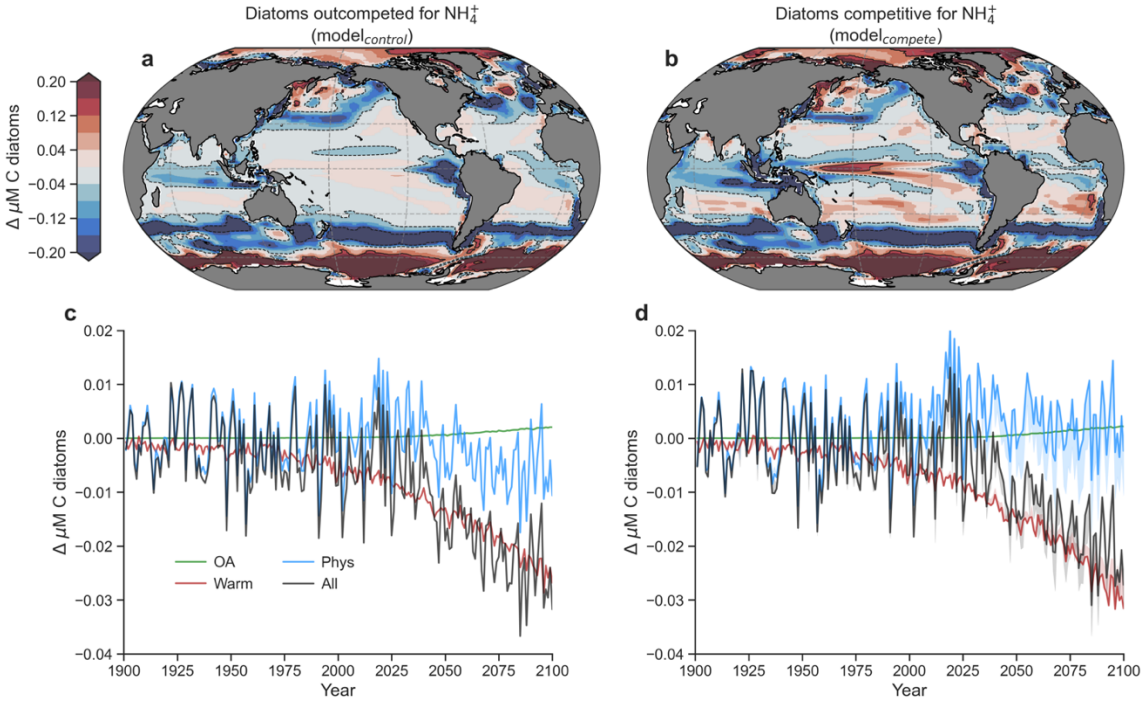

Figure S19. Impact of NH_4^+ enrichment within DIN on diatom abundance. (a), Mean change (Δ) in the abundance of diatoms (µM C) by the end of the 21st century (2081-2100) as predicted by the control run of the ocean-biogeochemical model ($model_{control}$) under the RCP8.5 scenario and averaged over the euphotic zone. (b), Same as in (a), but for the model with equal affinities of diatoms and other phytoplankton for NH_4^+ ($model_{compete}$). (c), Global mean change in diatom abundance due to physical (circulation + light) changes (blue), warming effects on metabolic rates (red), ocean acidification effect on ammonia oxidation (green) and all stressors (black) for $model_{control}$. (d), The same as in (c), but for $model_{compete}$. Shading shows the change between (c) and (d).

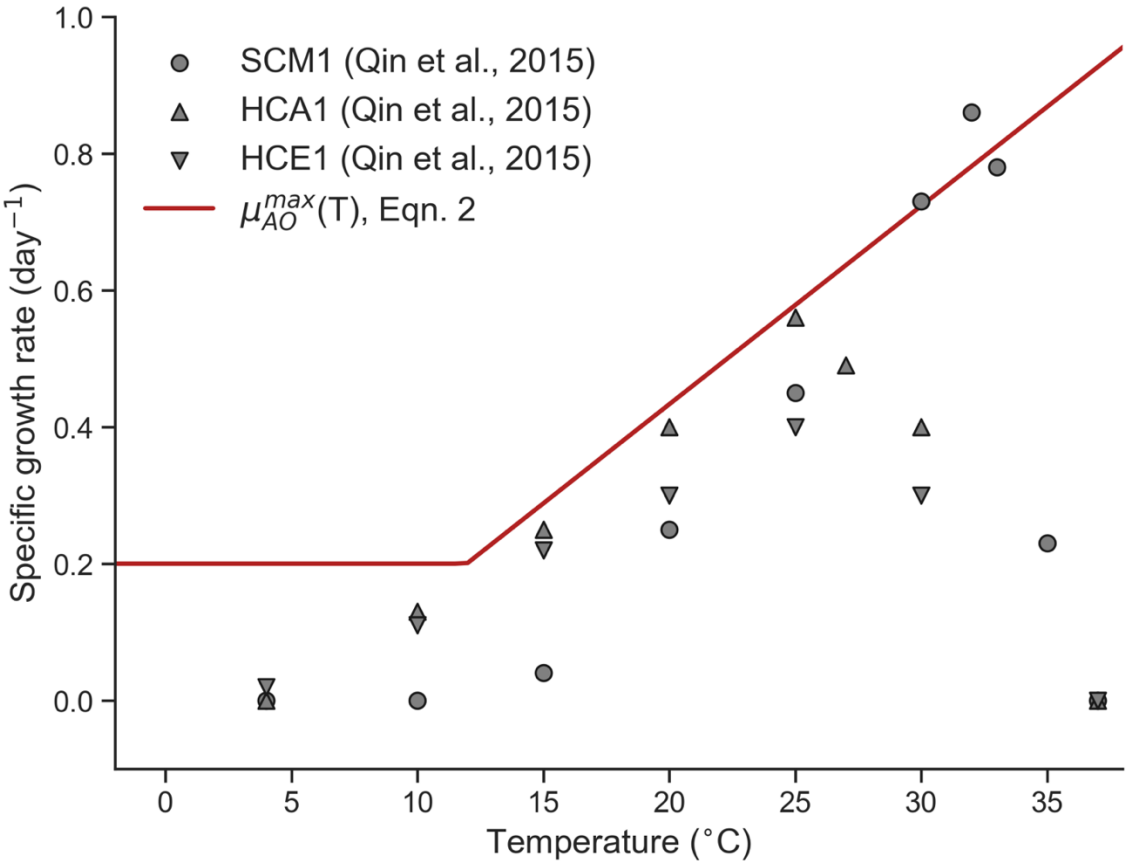

Figure S20. Temperature dependence of the maximum growth rate (μ) of ammonia oxidising archaea ecotypes (Qin et al., 2015).

significance	18S metabarcodes				
Predictor	**Model-derived**	**WOA**	***in situ***	**Darwin NH_4^+:DIN**	**Darwin + *in situ***
Si	***	ns	*	**	ns
NH_4^+:DIN	***	***	***	***	***
PO_4^{2-}	***	*	*	ns	**
dFe	ns	ns	*	ns	**
MLD	***	*	**	**	**
significance	***psbO* gene counts**				
Predictor	**Model-derived**	**WOA**	***in situ***	**Darwin NH_4^+:DIN**	**Darwin + *in situ***
Si	**	ns	ns	**	ns
NH_4^+:DIN	**	*	**	***	***
PO_4^{2-}	ns	**	**	ns	**
dFe	ns	**	***	ns	***
MLD	***	**	***	***	**
% Deviance explained	**18S metabarcodes**				
Predictor	**Model-derived**	**WOA**	***in situ***	**Darwin NH_4^+:DIN**	**Darwin + *in situ***
Si	24 (5)	21 (1)	17 (2)	24 (4)	17 (2)
NH_4^+:DIN	30 (16)	30 (4)	29 (7)	22 (6)	24 (2)
PO_4^{2-}	11 (8)	32 (3)	24 (3)	11 (1)	24 (4)
dFe	4 (0)	4 (1)	5 (5)	4 (2)	5 (4)
MLD	17 (6)	17 (3)	19 (5)	18 (5)	19 (5)
% Deviance explained	***psbO* gene counts**				
Predictor	**Model-derived**	**WOA**	***in situ***	**Darwin NH_4^+:DIN**	**Darwin + *in situ***
Si	25 (1)	17 (1)	13 (0)	25 (2)	13 (0)
NH_4^+:DIN	18 (2)	18 (2)	18 (3)	24 (4)	30 (3)
PO_4^{2-}	15 (0)	27 (4)	15 (4)	15 (0)	15 (3)
dFe	7 (1)	7 (6)	13 (13)	7 (0)	13 (8)
MLD	19 (9)	19 (5)	21 (7)	19 (6)	21 (6)

Table S1. Generalized Additive Model (GAM) results for predictions of the relative abundance of diatoms. Data provided by *Tara* Oceans 18S rRNA gene metabarcoding and *psbO* gene counts. Rows are the different predictor variables. Si = Silicate, PO_4^{2-} = Phosphate, dFe = dissolved iron, MLD = mixed layer depth. Significance is assessed by applying a smoothing penalty to the predictor in question. Deviance explained is calculated by fitting a GAM with only the predictor in question, and by removing the predictor from the full model and comparing the difference in deviance explained with the full model (this result is provided in the parantheses). The most significant or most

explanatory are highlighted. (*) p-value < 0.05. (**) p-value < 0.01. (***) p-value < 0.001.

18S metabarcodes		
Taxa	**Model-derived**	**Darwin model**
Diatoms	29.9% (***)	21.6% (***)
Cryptophytes	2.4%	4.3% (*)
Chlorophytes	2.6%	1.6%
Dinoflagellates	36.8% (***)	30.6% (***)
Haptophytes	4.3% (*)	5.9% (**)
Dictyochophytes	9.1% (**)	11.4% (***)
Pelagophytes	0.0%	6.8% (**)
***psbO* gene counts**		
Taxa	**Model-derived**	**Darwin model**
Diatoms	17.6 (***)	24.3% (***)
Prochlorococcus	23.4% (***)	16.0% (***)
Synechococcus	5.9% (**)	7.7% (**)
Chlorophytes	13.2% (***)	21.2% (***)
Dinoflagellates	1%	0.0%
Haptophytes	13.6% (***)	1.2%
Pelagophytes	11.2% (***)	12.5% (***)
Trichodesmium	4%	9.3% (**)
Other eukaryotes	0.1%	8.5% (**)

Table S2. Deviance explained from the Generalized Additive Models using NH_4^+:DIN as the sole predictor of the relative abundance of different eukaryotic phytoplankton taxa. Data provided by *Tara* Oceans 18S rRNA gene metabarcoding and *psbO* gene counts. Significance of NH_4^+:DIN as a predictor of diatom relative abundance is denoted by the number of *. No * means p-value > 0.05. (*) p-value < 0.05. (**) p-value < 0.01. (***) p-value < 0.001. NH_4^+:DIN may be model-derived from PISCES-v2 or from the Darwin model (Follows et al., 2007).

Parameter	Description	Value	Units
μ_{AO}^{max}	Maximum rate of ammonia oxidation	Eqn. 2	day^{-1}
$K_{AO}^{NH_4^+}$	Ammonia oxidation half-saturation constant for ammonium	0.1	$mmol\ m^{-3}$
K_{AO}^{PAR}	Ammonia oxidation half-saturation constant for photosynthetically active radiation	0.75	$W\ m^{-2}$
R_{AO}^{pH}	Reference pH below which ammonia oxidation is limited	8.0	pH units
pK_a	pH at which all NH_x is NH_3	9.3	pH units
μ_{NO}^{max}	Maximum rate of nitrite oxidation	0.15	day^{-1}
$K_{NO}^{NO_2^-}$	Nitrite oxidation half-saturation constant for nitrite	0.1	$\mu mol\ m^{-3}$
K_{NO}^{PAR}	Nitrite oxidation half-saturation constant for photosynthetically active radiation	0.75	$W\ m^{-2}$

Table S3. Parameters and their values used to simulate ammonia and nitrite oxidation in the PISCES-v2 ocean biogeochemical model, detailed in equations 1-8. Values are informed by field and laboratory studies cited in the methods.

Data Set S1. Nutrient concentration data.

Data Set S2. Ammonia oxidation rate data.

Data Set S3. Coincident nutrient and regenerated to new primary production rate data.

Data Set S4. Variations in ammonia oxidation rates for pH changes. Rates normalized to a pH of 8.